
When Muon Optimizer Meets Adversarial Training: A Theoretical and Empirical Study

Jun Yan¹
yanjun@ieee.org

Weiquan Huang²
weiquanh@tongji.edu.cn

Jiankai Zuo³
zuojiankai@usts.edu.cn

Yujian Mo²
yujmo@tongji.edu.cn

Xi Fang⁴
xifang@dp.tech

Chengliang Wu¹
clwu@shou.edu.cn

Zeming Wei⁵
weizeming@stu.pku.edu.cn

¹IT College, Shanghai Ocean University, Shanghai, 201306

²School of Computer Science and Technology, Tongji University, Shanghai, 201804

³SEIE, Suzhou University of Science and Technology, Suzhou, 215009

⁴DP Tech, Shanghai, 200030

⁵School of Mathematical Sciences, Peking University, Beijing, 100871

Abstract

Adversarial training (AT) remains one of the most reliable empirical defenses against adversarial attacks. Its robustness critically depends on how the underlying min-max objective is optimized. In practice, Stochastic Gradient Descent (SGD) optimizer remains the default optimization choice for AT, whereas adaptive optimizers often improve standard training but may yield inferior robustness. Recently, the Muon optimizer, which orthogonalizes matrix-valued updates via an approximate polar decomposition, has achieved notable success in large-scale training at a memory cost comparable to SGD. This raises a security-relevant question: *can orthogonalized optimization improve AT under strong and heterogeneous threat models?* Focusing on this problem, we conduct a comprehensive theoretical and empirical study. Theoretically, we show that Muon imposes a spectral-norm stability ceiling on matrix updates, limiting uncontrolled spectral growth in the training dynamics without explicitly shrinking the learned weights. Empirically, across five architectures and three ℓ_p threat models ($\ell_\infty, \ell_1, \ell_2$) and their union, Muon is competitive with SGD on CNNs and substantially outperforms AdamW on both CNNs and ViTs. These results identify optimizer geometry as a security-relevant factor in adversarial training, while clarifying the empirical regimes in which orthogonalized updates are beneficial. Overall, our findings highlight optimizer design as a security-critical component of AT.

1 Introduction

Deep neural networks are increasingly deployed in security-sensitive settings, yet their predictions can be manipulated by small, human-imperceptible adversarial perturbations [44, 22, 36, 9]. To mitigate such potential threats to neural networks, robust training methods known as adversarial training (AT) have been proposed [36, 52, 48, 14]. These methods are based on robust optimization, aiming to maximize adversarial perturbations while minimizing empirical risk.

The outer optimization problem in AT is often noisier and more ill-conditioned than standard empirical risk minimization, because each update is computed on adversarially perturbed inputs produced by an inner maximization procedure. In this regime, optimizer-induced geometry can have a non-negligible effect on both clean accuracy and robust accuracy. Adaptive optimizers such as Adam and AdamW

rescale each coordinate of the update by an estimate of its gradient second moment. The Stochastic Gradient Descent (SGD) optimizer and its momentum variants avoid this per-coordinate rescaling, and have been observed to yield greater robustness under the high-variance gradients of AT [15]. Empirical studies have also validated their superiority in AT [39]. Some studies have also focused on enhancing robustness by exploring the Sharpness-Aware Minimization (SAM) method, which perturbs model weights to seek a flatter loss landscape [53, 54]. These studies make the parameter dynamics of min-max optimization analytically tractable, allowing robustness gains to be attributed to specific update-rule properties (e.g., implicit regularization of curvature or spectral norms) rather than treated as emergent artifacts.

A previous study [39] found that the effectiveness of using Adam [29] or AdamW [34] in AT is suboptimal. Recently, the Muon optimizer [28] has been introduced, which avoids expensive high-order projection algorithms while exploiting orthogonalized update geometry and enables a large-batch-friendly update that can be efficiently approximated by a small fixed number of Newton-Schulz iterations. This optimization method constrains the update direction (the polar factor of the momentum-accumulated gradient) to the Stiefel manifold, yielding orthogonalized, spectrally balanced parameter updates (though the weights W_t themselves need not lie on the manifold) [31]. The Muon optimizer differs from other optimizers in that it orthogonalizes matrix-valued updates. For each 2D weight tensor, the Muon optimizer transforms the momentum update into its approximate polar factor, which can be realized via Newton-Schulz iterations. The updated geometry is fundamentally different from SGD [40, 8] and AdamW [34]. However, the impact of this optimizer on adversarial robustness remains unexplored.

To fill this research gap, we carry out a systematic theoretical and experimental study of the Muon optimizer in the AT paradigm, as illustrated in Figure 1. We first establish a theoretical mechanism and explanation linked to robustness. Intuitively, adversarial vulnerability is governed by norms of input gradients and Jacobians [27]. We show that Muon’s polar update induces a spectral-norm stability ceiling at the update level. Each matrix-valued update has a controlled operator norm after orthogonalization. This property does not directly enforce small spectral norms of the learned weights. Instead, it provides a mechanism for limiting abrupt spectral growth in the optimization trajectory, offering a diagnostic explanation for the robustness behavior observed in our experiments. Empirically, we first adapt the Muon optimizer for AT, then conduct comprehensive experiments across multiple datasets and model architectures, to evaluate the robustness of four widely used optimizers: SGD, AdamW, SAM, and Muon. Across this grid, we observe that optimizer choice can induce large and consistent shifts in the robustness frontier: the same training recipe can yield markedly different robustness profiles depending on optimization dynamics. In particular, the robustness gains provided by the Muon optimizer are significantly greater than those of AdamW, and Muon’s performance is competitive with SGD across multiple settings. Compared with SAM, Muon should be viewed as an optimizer-geometry alternative rather than a direct replacement. It improves update geometry without introducing an additional weight-perturbation step, but it does not uniformly dominate SAM in robustness. To summarize, our key empirical findings are: **(1)** Muon constrains the update geometry: each matrix-valued update has a bounded operator norm after polar orthogonalization. This does not imply that Muon always produces smaller weight spectral norms than SGD, but it helps prevent the unstable spectral growth often observed with adaptive optimizers such as AdamW. **(2)** On small-scale datasets like CIFAR-10 [30], Muon is on par with or superior to SGD on overparameterized CNNs [51]. On ViTs [18], Muon lags behind SGD yet remains markedly more stable and/or outperforms AdamW. However, on large-scale datasets like ImageNet [16], SGD still performs better, suggesting that sensitivity to large-scale learning rates is a key bottleneck, deserving future investigations. **(3)** Muon is an efficient optimizer-geometry alternative rather than a strict replacement for SAM.

Our contributions are summarized as follows:

- **Revisiting optimizer choice as a security-relevant factor in AT.** We identify orthogonalized matrix-update geometry as an underexplored factor in adversarial training and study Muon as a representative optimizer beyond the conventional SGD/AdamW/SAM comparison.
- **Mechanistic analysis of Muon’s spectral update geometry.** We analyze Muon’s polar update rule and show that it imposes an operator-norm ceiling on matrix-valued updates. We further relate this update-level constraint to spectral growth and nuclear-norm descent under adversarial loss dynamics, clarifying both what Muon can and cannot guarantee.

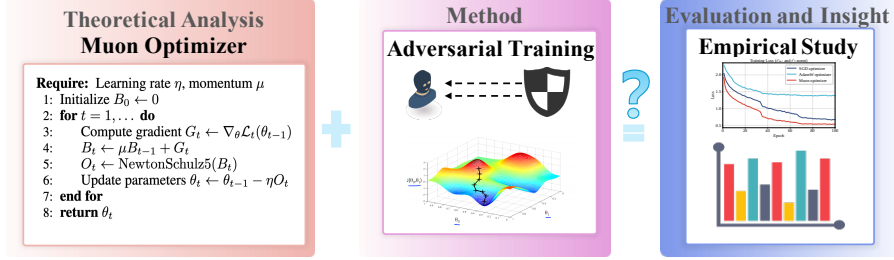


Figure 1: The framework of this study. The left part of the figure is adapted from the work [28].

- **Controlled multi-norm robustness evaluation.** We conduct a controlled empirical comparison of SGD, AdamW, and Muon across multiple architectures, datasets, and threat norms. We further include representative SAM comparisons on WideResNet-34-10 (WRN-34-10) [51] and ViT-B [19] to clarify the trade-off between orthogonalized updates and sharpness-aware perturbation-based optimization. Our results show that Muon often improves over AdamW and is competitive with SGD in several small-scale settings, while also exposing its scaling limitations on larger datasets.
- **Threat model and scope.** We consider standard test-time adversarial robustness under white-box ℓ_p -bounded attacks. The attacker has full access to the deployed classifier and its gradients, but the proposed method changes only the training-time optimizer. At inference time, the neural networks do not require gradient masking to increase robustness. We evaluate black box migration attacks to adapt to real-world security risks.

2 Theoretical Analysis

2.1 Preliminaries

Adversarial Training (AT). Let $f_\theta : \mathcal{X} \rightarrow \mathbb{R}^K$ denote a classifier parameterized by θ , with logits $g_\theta(x)$ and a classification margin $m_\theta(x, y) := g_\theta(x)_y - \max_{y' \neq y} g_\theta(x)_{y'}$. AT solves the min-max problem

$$\min_{\theta} \mathbb{E}_{(x,y) \sim \mathcal{D}} \left[\max_{\delta \in \Delta} \ell(f_\theta(x + \delta), y) \right], \quad (1)$$

where $\ell(\cdot, \cdot)$ is the classification loss.

Threat model. We consider the union of multiple ℓ_p threat models. Given a set of norms $\mathcal{P} \subseteq \{1, 2, \infty\}$ with per-norm radii $\{\varepsilon_p\}_{p \in \mathcal{P}}$, the perturbation set is

$$\Delta_{\text{union}} := \bigcup_{p \in \mathcal{P}} \{\delta \in \mathbb{R}^d : \|\delta\|_p \leq \varepsilon_p\}. \quad (2)$$

Muon update rule. For each 2D weight block $W_t \in \mathbb{R}^{m \times n}$, let $G_t = \nabla_W \mathcal{L}_{\text{adv}}(\theta_{t-1})$ denote the AT gradient and $M_t = \mu M_{t-1} + G_t$ the momentum-accumulated gradient. Muon applies the orthogonalized update

$$U_t = \text{polar}(M_t), \quad W_{t+1} = (1 - \eta\lambda)W_t - \eta U_t, \quad (3)$$

where $\eta > 0$ is the learning rate, $\lambda \geq 0$ is weight decay, and $\text{polar}(\cdot)$ is approximated by a fixed number of Newton–Schulz iterations (see Algorithm 2).

Notation. We use $\|\cdot\|_2$ for the spectral (operator-2) norm, $\|\cdot\|_F$ for the Frobenius norm, $\|\cdot\|_*$ for the nuclear norm, and $\sigma_i(\cdot)$ for singular values. $J_f(x)$ denotes the Jacobian of f at x . Per-layer weights are W_ℓ with spectral norm upper bound B_ℓ (to be established in Theorem 2.1). We analyze how the update rule of Eq. (3) governs $\|W_\ell\|_2$, the Lipschitz constant of m_θ , and the per-step descent on the AT objective defined in Eq. (1).

2.2 Spectral-Norm Stability Ceiling

This section proves that Muon’s polar update admits a spectral-norm stability ceiling (Theorem 2.1). Theoretically, we show that Muon’s polar update imposes a spectral-norm stability ceiling on each

matrix update, preventing the unbounded spectral growth seen with adaptive optimizers. It is a structural property rather than a tight robustness certificate.

Proposition 2.1 (Robustness governed by the dual norm of input gradients). *Under a first-order Taylor expansion of m_θ ,*

$$m_\theta(x + \delta, y) \approx m_\theta(x, y) + \langle \nabla_x m_\theta(x, y), \delta \rangle.$$

Hence by Hölder's inequality with $1/p + 1/q = 1$,

$$\max_{\|\delta\|_p \leq \varepsilon} |m_\theta(x + \delta, y) - m_\theta(x, y)| = \varepsilon \|\nabla_x m_\theta(x, y)\|_q,$$

so robustness at x is approximate to $m_\theta(x, y) > \varepsilon \|\nabla_x m_\theta(x, y)\|_q$.

Appendix C provides the remark of Proposition 2.1.

Proposition 2.2 (Bounding the input Jacobian with layer spectral norms). *For a feedforward network $f(x) = W_L \phi(\dots \phi(W_1 x))$ with L layers, if the activations ϕ are 1-Lipschitz (e.g., ReLU, leaky-ReLU), then*

$$\|J_f(x)\|_2 \leq \prod_{\ell=1}^L \|W_\ell\|_2. \quad (4)$$

This gives $\|\nabla_x g_\theta(x)\|_2 \leq C \cdot \prod_{\ell} \|W_\ell\|_2$, where C absorbs activation Lipschitz constants and output projections.

The Muon optimizer uses the Newton–Schulz approximation for polar decomposition [28], whose update rule is defined in Eq. (3). The polar factor is an approximately orthogonal matrix with a spectral norm of 1. The following lemma extends prior analysis [28, 26].

Lemma 2.1. *Let $A \in \mathbb{R}^{m \times n}$ be full rank with compact SVD $A = P\Sigma V^\top$, and define $\text{Ortho}(A) = PV^\top$. Then $\|\text{Ortho}(A)\|_2 = 1$. Moreover, if $m \geq n$,*

$$\text{Ortho}(A)^\top \text{Ortho}(A) = I_n, \quad A = \text{Ortho}(A)(A^\top A)^{1/2}; \quad (5)$$

if $m < n$, we have $\text{Ortho}(A) \text{Ortho}(A)^\top = I_m$, $A = (AA^\top)^{1/2} \text{Ortho}(A)$. Equivalently, $\text{Ortho}(A)$ is the Frobenius projection of A onto the corresponding rectangular Stiefel set.

The proof of Lemma 2.1 is given in Appendix D.1.

Theorem 2.1. *Assume there is a quantifiable orthogonalization error $\varepsilon_t \geq 0$, such that*

$$\|\tilde{U}_t\|_2 \leq 1 + \varepsilon_t. \quad (6)$$

The ideal Muon optimizer (exact polar) corresponds to $\varepsilon_t = 0$, while the finite-step Newton–Schulz approximate polar factor corresponds to a small value $\varepsilon_t > 0$.

Under the assumption of Eq. (6) and $0 \leq \eta\lambda \leq 1$, for any $t \geq 0$, the spectral norm satisfies the following recursive upper bound

$$\|W_{t+1}\|_2 \leq (1 - \eta\lambda) \|W_t\|_2 + \eta(1 + \varepsilon_t). \quad (7)$$

Furthermore, if $\eta\lambda \in (0, 1)$, the following explicit trajectory upper bound holds

$$\|W_t\|_2 \leq (1 - \eta\lambda)^t \|W_0\|_2 + \frac{1 - (1 - \eta\lambda)^t}{\lambda} + \eta \sum_{k=0}^{t-1} (1 - \eta\lambda)^{t-1-k} \varepsilon_k. \quad (8)$$

Specifically, if $\varepsilon_t \leq \bar{\varepsilon}$ for all t , then, it satisfies

$$\|W_t\|_2 \leq (1 - \eta\lambda)^t \|W_0\|_2 + \frac{1 + \bar{\varepsilon}}{\lambda} (1 - (1 - \eta\lambda)^t) \leq \max \left\{ \|W_0\|_2, \frac{1 + \bar{\varepsilon}}{\lambda} \right\}. \quad (9)$$

Appendix C provides the remark of Theorem 2.1. The proof of Theorem 2.1 is given in Appendix D.2.

Theorem 2.2. Fix $\mathcal{P} \subseteq \{1, 2, \infty\}$ with radii $\{\varepsilon_p\}_{p \in \mathcal{P}}$ and let $\Delta_{\text{union}} = \bigcup_{p \in \mathcal{P}} \{\delta \in \mathbb{R}^d : \|\delta\|_p \leq \varepsilon_p\}$. Suppose every layer satisfies $\|W_\ell\|_2 \leq B_\ell$ (as guaranteed by Theorem 2.1 with weight decay $\lambda > 0$), and define

$$\hat{L}_p(\theta) := c_p C_{\text{marg}} \prod_{\ell=1}^L B_\ell, \quad C_{\text{marg}} := \max_{j \neq y} \|e_y - e_j\|_2 = \sqrt{2}. \quad (10)$$

where c_p is the norm-equivalence constant satisfying $\|\delta\|_2 \leq c_p \|\delta\|_p$ for all $\delta \in \mathbb{R}^d$ (concretely, $c_\infty = \sqrt{d}$, $c_2 = 1$, and $c_1 = 1$, since $\|\delta\|_2 \leq \sqrt{d} \|\delta\|_\infty$ and $\|\delta\|_2 \leq \|\delta\|_1$). Furthermore, C_{marg} absorbs the output-layer projection from logits to margin. If

$$m_\theta(x, y) > \max_{p \in \mathcal{P}} \hat{L}_p(\theta) \varepsilon_p, \quad (11)$$

then $m_\theta(x + \delta, y) > 0$ for all $\delta \in \Delta_{\text{union}}$.

Appendix C provides the remark of Theorem 2.2. The proof of Theorem 2.2 is given in Appendix D.3.

2.3 Muon’s Gradient Dynamics under Min-Max Optimization

Our main result (Theorem 2.3) shows that Muon descends the adversarial loss along the nuclear-norm direction with a structurally larger per-step guarantee than SGD.

Assumption 2.1. We can view the adversarial loss L_{adv} as a function $F(W)$ of a particular weight block W . Assume that F is β -smooth, i.e., the following inequality holds

$$F(W + \Delta) \leq F(W) + \langle \nabla F(W), \Delta \rangle + \frac{\beta}{2} \|\Delta\|_F^2, \quad (12)$$

where Δ represents any perturbation or increment to the parameter block W .

Theorem 2.3 (Muon optimizer on the adversarial loss for the min-max dynamics). *In AT, assume F is β -smooth w.r.t. $\|\cdot\|_F$. Let $G = \nabla_W F(W)$ be the block gradient and let M be the momentum-accumulated gradient used by Muon. Let \tilde{U} be the inexact polar direction used in practice, satisfying*

$$\|\tilde{U} - \text{Ortho}(M)\|_F \leq \delta_{\text{orth}}, \quad \|\tilde{U}\|_2 \leq 1 + \varepsilon, \quad \|\tilde{U}\|_F^2 \leq r(1 + \varepsilon)^2, \quad (13)$$

where r is $\text{rank}(M)$ or any upper bound on it. Consider the update $W^+ = W - \eta \tilde{U}$ with $\eta > 0$. Then the following inequality holds:

$$F(W^+) \leq F(W) - \eta \|M\|_* + \eta(1 + \varepsilon) \|G - M\|_* + \eta \sqrt{r} \|M\|_2 \delta_{\text{orth}} + \frac{\beta}{2} \eta^2 r(1 + \varepsilon)^2. \quad (14)$$

Appendix C provides the remark of Theorem 2.3. The proof of Theorem 2.3 is given in Appendix D.4.

3 Empirical Results and Insights

3.1 Adapting Muon for AT

We adopt an AT method derived from a previous seminal work [14]. We instantiate the AT objective defined in Eq. (1) with APGD as the inner attack and Muon as the outer optimizer.

The attack method used in our study is Auto Projected Gradient Descent (APGD) [13]. It replaces the fixed step size of PGD with an adaptive schedule and an automatic restart mechanism. For ℓ_∞ and ℓ_2 attacks, it uses $\text{sign}(\nabla_x \ell)$ and $\nabla_x \ell / \|\nabla_x \ell\|_2$, respectively. For the ℓ_1 attack, the step ascends along the top- k coordinates of $|\nabla_x \ell|$ (a sparse steepest-ascent direction) and projects the iterate back onto the ℓ_1 ball of radius ε_1 after each step [14].

Algorithm 1 outlines the AT procedure. We sample a norm per mini-batch (e.g., ℓ_∞ or ℓ_1) to craft adversarial examples, then update the model parameters. Various optimizers can be integrated as plugins within this AT framework.

Algorithm 1 Multi-Norm APGD Adversarial Training

Require: Model f_θ , data loader \mathcal{D} , threat norms $\mathcal{P} = \{p_1, \dots, p_M\}$, radii $\{\varepsilon_i\}_{i=1}^M$, attack steps $\{T_i\}_{i=1}^M$, optimizer Opt (SGD / AdamW / Muon), adversarial loss $\ell(\cdot, \cdot)$, optional scheduler Scheduler

```
1: Initialize parameters  $\theta$  (random or pretrained)
2: for epoch = 1 to  $K$  do
3:   for each minibatch  $(x, y) \sim \mathcal{D}$  do
4:      $i \leftarrow \text{SampleThreatIndex}(\{1, \dots, M\})$ 
5:      $p \leftarrow p_i, \varepsilon \leftarrow \varepsilon_i, T \leftarrow T_i$ 
6:      $x_{\text{adv}} \leftarrow \text{APGD}(f_\theta, x, y; p, \varepsilon, T, \ell)$ 
7:     Opt.zero_grad()
8:      $L_{\text{adv}} \leftarrow \ell(f_\theta(x_{\text{adv}}), y)$ 
9:     Backprop( $L_{\text{adv}}$ )
10:    Opt.step() ▷ If Muon: see Alg. 2 for the expanded step
11:    if Scheduler is used then
12:      Scheduler.step()
13:    end if
14:  end for
15: end for
```

3.2 Experiment Setup

Datasets. The CIFAR-10 dataset [30] is a commonly used dataset in computer vision. It consists of 60,000 32×32 color images in 10 classes with 50,000 training images and 10,000 test images. It is a standard benchmark in adversarial robustness research. ImageNet [16] is a large-scale image database for visual recognition research. It contains over 14 million human-annotated images spanning more than 20,000 categories, and around 1 million images include object bounding boxes. In research practice, the dataset is often used in its 1,000-class subset, which includes 1,281,167 training samples and 50,000 validation samples.

Training Details. On CIFAR-10 [30], the training process lasts for 100 epochs. The APGD method [13] is used as the default attack method with 10 iteration steps. For the ℓ_∞ -attack, the perturbation budget is $\varepsilon_\infty = \frac{8.0}{255.0}$. For the ℓ_2 -attack, the perturbation budget is $\varepsilon_2 = 0.5$. For the ℓ_1 -attack, the perturbation budget is $\varepsilon_1 = 12$. The batch size is set to 128. For CNNs [24, 51], the initial learning rate is 1.0. For ViTs [18], the initial learning rate is 0.001. The learning rate is set in a stepwise manner, decreasing to 0.1 and 0.01 of the initial learning rate at 1/3 and 2/3 of the entire training period, respectively. The momentum coefficient μ is 0.9, and the weight decay λ is 0.0005. On ImageNet [16], the training process lasts for 100 epochs. Due to computing resource constraints, the defense is only deployed on ResNet-50 [23]. The AT mode is set to the $\ell_\infty + \ell_1$ joint norm. The batch size is still set to 128. For the ℓ_∞ -attack, the perturbation budget is $\varepsilon_\infty = \frac{4.0}{255.0}$, and the attack step number is 5. For the ℓ_2 -attack, the perturbation budget is $\varepsilon_2 = 2$, and the attack step number is 10. For the ℓ_1 -attack, the perturbation budget is $\varepsilon_1 = 255$, and the attack step number is 15.

3.3 Main Evaluation Results on CIFAR-10

The models selected for our experiment include PreActResNet-18 [24], WRN-34-10 [51], WRN-34-20 [51], ViT-B [18], and ViT-L [18]. The selection of best weights is based on their ℓ_∞ robustness. In practice, the best checkpoint is selected using a small validation subset during training, and the final reported performance is evaluated on the full test set. This protocol may introduce checkpoint-selection bias. We compare Muon [28], AdamW [34], and SGD [40, 8] on NVIDIA RTX 4080S.

PreActResNet-18. Table 1 shows the results on PreActResNet-18 (11.2 million parameters) [24]. Under the multi-norm training ($\ell_\infty + \ell_1$), Muon’s best checkpoint achieves the union robustness of 39.27, compared to SGD’s 40.37 and AdamW’s 36.53. Its robustness is optimal only under the ℓ_2 -norm training setting. On shallower CNNs, Muon is not necessarily superior to SGD. Muon’s advantage mainly lies in its balanced performance across norms.

WideResNet. Table 2 illustrates the robustness evaluation results on WRN-34-10 (48.2 million parameters) [51]. Muon achieves the strongest union robustness under AT. With ℓ_∞ -only training,

Table 1: AT results on PreActResNet-18 [24].

Norm	Opt.	Best					Last				
		Clean	ℓ_∞	ℓ_2	ℓ_1	Union	Clean	ℓ_∞	ℓ_2	ℓ_1	Union
$\ell_\infty + \ell_1$	SGD	79.21	40.84	64.86	52.15	40.37	81.22	35.77	64.16	48.00	35.07
	AdamW	66.26	36.83	55.19	45.59	36.53	69.98	32.78	55.36	43.76	32.38
	Muon	77.48	39.67	63.08	51.03	39.27	84.81	38.58	67.24	50.90	37.83
ℓ_∞	SGD	78.60	45.81	58.20	8.05	8.05	82.37	41.73	57.17	5.80	5.79
	AdamW	65.18	39.64	47.76	10.07	10.07	69.22	38.63	48.96	7.87	7.87
	Muon	78.04	43.86	58.58	10.16	10.16	85.74	43.68	60.84	6.00	6.00
ℓ_1	SGD	84.08	17.10	59.15	53.05	17.10	84.08	16.98	59.34	53.20	16.98
	AdamW	71.50	21.83	54.64	49.62	21.83	79.36	19.09	54.36	49.68	19.09
	Muon	76.30	23.63	57.75	51.71	23.63	86.68	18.19	63.50	57.57	18.19
ℓ_2	SGD	87.58	25.91	65.53	25.00	20.52	87.74	22.81	63.46	22.73	17.82
	AdamW	80.74	24.58	58.84	25.42	19.97	82.48	23.31	58.92	24.11	18.66
	Muon	85.10	28.52	64.09	27.75	22.85	89.66	23.82	66.94	25.75	19.63

Table 2: AT results on WRN-34-10 [51].

Norm	Optimizer	Best					Last				
		Clean	ℓ_∞	ℓ_2	ℓ_1	Union	Clean	ℓ_∞	ℓ_2	ℓ_1	Union
$\ell_1 + \ell_\infty$	SGD	78.19	38.18	63.29	50.51	37.74	81.52	32.03	61.43	43.71	31.36
	AdamW	75.43	37.80	60.42	47.49	37.15	78.90	35.72	61.48	46.57	34.99
	Muon	73.27	38.87	58.44	45.73	37.89	85.21	38.14	65.13	46.58	37.09
ℓ_∞	SGD	80.02	44.11	57.73	7.95	7.95	82.50	37.23	53.21	5.69	5.69
	AdamW	69.92	42.47	49.69	4.41	4.41	72.39	41.38	48.25	3.18	3.18
	Muon	83.16	46.71	58.11	4.88	4.88	85.96	43.81	54.05	4.34	4.34
ℓ_1	SGD	47.59	19.39	36.99	33.27	19.39	83.90	16.80	58.03	51.04	16.80
	AdamW	65.26	23.49	50.97	46.03	23.49	75.77	20.91	55.29	49.41	20.91
	Muon	78.81	24.89	58.87	53.56	24.89	87.83	19.60	63.03	58.15	19.60
ℓ_2	SGD	76.59	22.72	54.04	23.72	18.87	87.51	21.49	62.31	24.65	18.18
	AdamW	73.40	24.07	51.93	24.18	19.90	86.17	21.65	61.15	19.38	15.75
	Muon	89.97	26.85	68.16	25.96	21.63	90.18	26.44	68.56	26.59	21.53

Muon attains a high ℓ_∞ robust accuracy (46.71), but its ℓ_1 robustness nearly collapses (4.88). It reflects a general phenomenon where training against a single threat model tends to produce robustness mainly against that specific threat. Table 3 further shows robustness evaluation results on WRN-34-20 (192.9 million parameters) [51]. Muon’s best checkpoint achieves a union robustness of 39.15. Furthermore, the Muon optimizer attains higher ℓ_∞/ℓ_2 robustness (39.99/61.22). Under both $\ell_\infty + \ell_1$ and ℓ_∞ AT with the Muon optimizer, the ℓ_1 robust accuracy of the final checkpoint drops sharply, indicating that Muon needs an early-stopping strategy to mitigate “robust overfitting”.

Vision Transformers. Table 4 shows the robustness of ViT-B (85.7 million parameters) [18] under different optimizers. Muon is clearly beneficial for AT on ViT-B. Compared with AdamW, Muon substantially improves the stability of AT for Transformers. While SGD can also achieve a certain level of robustness on ViT-B, Muon’s advantage is that it remains relatively stable across AT scenarios. Single-norm training still specializes to its own threat for all optimizers. The distinction is that Muon avoids the training instability that plagues AdamW on Transformers. Table 5 shows the robustness of ViT-L (303.1 million parameters) [18] under different optimizers. The experimental observations on ViT-L are similar to those on ViT-B. On ViT-L, AdamW exhibits partial training failure, analogous to what happens when training ViT-B under the ℓ_∞ -norm. To stabilize AT with AdamW, we set the learning rate to 0.00005 and the weight decay to 0.02. We find that AdamW’s final model under ℓ_∞ -only training on ViT-L is close to random performance (e.g., the union robust accuracy is low),

Table 3: AT results on WRN-34-20 [51].

Norm	Optimizer	Best					Last				
		Clean	ℓ_∞	ℓ_2	ℓ_1	Union	Clean	ℓ_∞	ℓ_2	ℓ_1	Union
$\ell_1 + \ell_\infty$	SGD	75.35	36.84	59.99	48.18	36.51	82.58	34.14	62.16	44.79	33.26
	AdamW	72.39	35.44	57.51	43.99	34.65	72.39	35.43	57.51	44.04	34.63
	Muon	76.41	39.99	61.22	47.68	39.15	86.51	37.87	61.69	11.10	11.10
ℓ_∞	SGD	75.98	41.12	55.09	8.30	8.30	83.62	39.17	54.40	5.34	5.34
	AdamW	73.37	42.59	48.31	2.48	2.48	75.17	40.91	47.35	2.22	2.22
	Muon	82.13	46.58	57.98	5.30	5.30	87.44	46.76	56.99	5.15	5.15
ℓ_1	SGD	56.49	21.24	41.95	37.74	21.24	85.31	17.94	60.45	54.45	17.94
	AdamW	68.56	21.79	52.11	47.44	21.79	82.03	17.37	57.17	50.30	17.37
	Muon	88.53	21.45	65.71	60.19	21.45	88.61	20.83	65.16	59.95	20.83
ℓ_2	SGD	88.33	24.37	64.29	25.26	20.11	88.48	23.93	64.84	25.66	20.05
	AdamW	85.55	22.73	61.20	22.15	17.92	85.45	22.59	60.76	21.53	17.76
	Muon	91.09	28.15	70.14	27.26	22.64	91.16	27.84	70.38	27.25	22.44

Table 4: AT results on ViT-B [18].

Norm	Optimizer	Best					Last				
		Clean	ℓ_∞	ℓ_2	ℓ_1	Union	Clean	ℓ_∞	ℓ_2	ℓ_1	Union
$\ell_1 + \ell_\infty$	SGD	66.35	29.64	52.69	44.78	29.62	71.96	24.88	52.94	40.32	24.80
	AdamW	27.22	12.10	18.97	16.54	12.02	32.77	13.62	23.11	19.88	13.53
	Muon	61.53	27.03	48.63	42.61	27.03	65.49	19.17	45.79	35.42	19.15
ℓ_∞	SGD	64.65	30.97	50.42	32.59	28.10	71.64	26.15	52.58	27.86	27.71
	AdamW	17.93	12.12	11.60	4.48	4.48	17.25	12.93	12.31	5.77	5.77
	Muon	60.66	30.36	47.20	28.00	25.73	66.26	19.93	44.20	26.23	19.30
ℓ_1	SGD	68.48	22.63	51.30	45.27	22.63	72.24	17.19	49.72	43.06	17.19
	AdamW	25.57	8.99	17.08	15.94	8.97	28.26	6.47	16.98	15.66	6.44
	Muon	58.58	21.15	44.41	40.93	21.15	64.64	12.15	40.61	34.79	12.15
ℓ_2	SGD	57.08	17.49	40.32	29.44	17.48	76.50	18.61	52.99	33.55	18.46
	AdamW	18.51	11.53	13.95	13.01	11.49	35.10	8.81	20.54	16.13	8.71
	Muon	58.49	17.66	41.01	31.77	17.62	67.89	12.70	42.60	30.96	12.70

whereas Muon still maintains considerable robustness. However, AT with Muon can also suffer from “robust overfitting”.

In summary, AT with the Muon optimizer achieves considerable robustness on overparameterized CNNs. Muon achieves union robustness on par with or better than SGD on WRN-34-10/20, while outperforming AdamW by a large margin. On ViT-B and ViT-L, both Muon and SGD yield stable AT, while AdamW may collapse to near-random performance. Muon offers the most consistent ℓ_∞ robustness among the three, whereas SGD remains competitive on union robustness.

3.4 Discussion

Robust Overfitting. We observe the symptom of “robust overfitting” in the experiments. It indicates that Muon improves optimization stability in some cases but does not eliminate the late-stage robustness degradation. It suggests that the “early stopping” strategy remains important for Muon-based AT as well as for SGD-based AT. We discuss the experimental phenomenon in Appendix G.

Training Time. Table 6 reports the AT time across different optimizers. We train WRN-34-20 for 100 epochs. The training time is comparable across the three optimizers.

Table 5: AT results on ViT-L [18].

Norm	Optimizer	Best					Last				
		Clean	ℓ_∞	ℓ_2	ℓ_1	Union	Clean	ℓ_∞	ℓ_2	ℓ_1	Union
$\ell_1 + \ell_\infty$	SGD	69.87	32.51	55.86	47.39	32.50	73.10	26.69	55.09	43.03	26.64
	AdamW	26.52	11.43	19.14	16.28	11.23	25.10	10.62	17.12	15.19	10.59
	Muon	63.85	28.18	50.85	43.94	28.18	68.02	21.65	47.79	37.25	21.64
ℓ_∞	SGD	70.15	34.26	55.30	34.95	30.25	72.32	25.61	51.95	27.67	22.68
	AdamW	16.98	12.85	14.12	10.41	10.32	18.05	6.13	8.14	0.79	0.65
	Muon	60.42	31.79	47.76	28.72	26.61	68.35	23.03	48.16	27.52	21.95
ℓ_1	SGD	24.68	9.22	18.22	18.58	9.22	40.60	13.48	29.27	28.23	13.48
	AdamW	17.84	11.12	14.90	14.83	11.12	24.27	5.62	13.27	13.02	5.62
	Muon	58.00	21.13	43.75	39.80	21.13	67.47	14.05	44.00	39.09	14.05
ℓ_2	SGD	77.03	18.37	55.32	33.31	18.15	77.22	19.01	54.40	34.42	18.78
	AdamW	21.31	10.24	16.63	14.63	10.24	26.38	5.77	14.80	11.62	5.73
	Muon	67.40	21.40	48.68	35.54	21.33	71.17	15.32	46.74	31.90	15.26

Table 6: Training time for WRN-34-20 [51] under different threat norms. Times are converted from seconds to hours (h) and minutes (m), rounded to the nearest minute.

Metric	SGD				AdamW				Muon			
	$\ell_1 + \ell_\infty$	ℓ_∞	ℓ_1	ℓ_2	$\ell_1 + \ell_\infty$	ℓ_∞	ℓ_1	ℓ_2	$\ell_1 + \ell_\infty$	ℓ_∞	ℓ_1	ℓ_2
Time	51h59m	51h47m	52h18m	51h49m	52h06m	51h52m	52h21m	51h56m	52h45m	52h29m	53h04m	52h32m

Table 7: AT results on WRN-34-10 and ViT-B (SAM vs. Muon).

Model	Norm	Optimizer	Best					Last				
			Clean	ℓ_∞	ℓ_2	ℓ_1	Union	Clean	ℓ_∞	ℓ_2	ℓ_1	Union
WRN-34-10	$\ell_1 + \ell_\infty$	SAM	78.75	40.98	64.64	52.77	40.64	80.93	40.93	65.84	52.71	40.52
		Muon	73.27	38.87	58.44	45.73	37.89	85.21	38.14	65.13	46.58	37.09
	ℓ_∞	SAM	80.53	46.08	60.30	10.43	10.43	81.84	46.20	60.76	9.74	9.73
		Muon	83.16	46.71	58.11	4.88	4.88	85.96	43.81	54.06	4.34	4.34
	ℓ_1	SAM	83.93	24.87	63.78	57.57	24.86	85.04	22.34	63.92	57.66	22.34
		Muon	78.81	24.89	58.87	53.56	24.89	87.83	19.60	63.03	58.15	19.60
ℓ_2	SAM	87.95	29.27	67.50	29.34	24.23	89.28	25.76	67.49	26.62	21.21	
	Muon	89.97	26.85	68.16	25.96	21.63	90.18	26.44	68.56	26.59	21.53	
ViT-B	$\ell_1 + \ell_\infty$	SAM	56.48	28.05	45.24	40.01	28.04	57.83	28.99	46.35	41.19	28.99
		Muon	61.53	27.03	48.63	42.61	27.03	65.49	19.17	45.79	35.42	19.15
	ℓ_∞	SAM	51.70	28.08	40.76	24.79	23.44	51.88	28.52	40.99	24.83	23.66
		Muon	60.66	30.36	47.20	28.00	25.73	66.26	19.93	44.20	26.23	19.30
	ℓ_1	SAM	66.03	24.65	50.57	46.24	24.65	67.63	25.26	52.11	47.21	25.26
		Muon	58.58	21.15	44.41	40.93	21.15	64.64	12.15	40.61	34.79	12.15
ℓ_2	SAM	75.30	24.98	55.97	37.28	24.57	75.45	24.91	56.33	37.17	24.49	
	Muon	58.49	17.66	41.01	31.77	17.62	67.89	12.70	42.60	30.96	12.70	

Comparison with SAM. We conduct a comparison experiment between Muon and SAM ($\rho = 0.05$) on WRN-34-10 (WRN-34-10) [51] and ViT-B [18]. Table 7 demonstrates the robustness advantage of the SAM optimizer. Nevertheless, SAM requires two backpropagations. Taking ℓ_2 -norm AT on WRN-34-10 as an example, SAM takes 67,741.1 s, while Muon requires only 60,415.0 s.

Results on ImageNet. Although AT on ImageNet [16] incurs substantial overhead, the exploration is still meaningful. We find that SGD admits a large initial learning rate (e.g., 1.0) on ResNet-50 [23], whereas Muon and AdamW require a smaller initial learning rate (0.0001). We test 2,000 samples

Table 8: Results on the ImageNet validation set [16].

Optimizer	Best					Last				
	Clean	ℓ_∞	ℓ_2	ℓ_1	Union	Clean	ℓ_∞	ℓ_2	ℓ_1	Union
SGD	56.02	22.22	37.30	23.63	20.17	51.03	8.40	23.39	11.72	7.76
AdamW	42.43	7.62	17.87	2.88	2.49	42.09	7.28	18.41	9.18	6.35
Muon	48.44	19.04	31.45	18.12	16.21	50.93	9.33	16.80	2.98	2.50

from the validation set. Table 8 shows that SGD performs best among the tested optimizers under our current hyperparameters and compute budgets on ImageNet. We do not interpret this result as ruling out Muon-based AT at scale. Rather, it suggests that Muon is more sensitive to learning rate, warmup, and weight decay choices at scale [32]. Further ImageNet-scale tuning on Muon-based AT is needed before drawing definitive conclusions.

4 Conclusion

The proposal of the Muon optimizer has opened up a new paradigm for robustness research: can this optimizer, which orthogonalizes updates via polar decomposition, achieve effects comparable to gradient descent optimizers in driving robustness? From a theoretical perspective, we connect Muon’s orthogonalized updates to a spectral-norm stability ceiling and a per-step nuclear-norm descent guarantee, characterizing the optimization dynamics induced by min-max training. The experimental results show that the Muon optimizer converges faster under AT (see Appendix F). On CIFAR-10, iMuon is consistently stronger than AdamW and is competitive with SGD across many CNN and ViT settings, but it does not uniformly dominate SGD. Its main benefit is not a universal robustness improvement, but a stable orthogonalized update geometry that often improves early robust optimization. On ImageNet, our pilot study shows that SGD remains stronger under the current tuning budget, indicating that large-scale Muon-based AT requires further hyperparameter and schedule design.

References

- [1] Zeyuan Allen-Zhu and Yuanzhi Li. Feature purification: How adversarial training performs robust deep learning. In *IEEE 62nd annual symposium on foundations of computer science (FOCS)*, pages 977–988, 2022.
- [2] Maksym Andriushchenko and Nicolas Flammarion. Understanding and improving fast adversarial training. *Advances in Neural Information Processing Systems*, 33:16048–16059, 2020.
- [3] Maksym Andriushchenko and Nicolas Flammarion. Towards understanding sharpness-aware minimization. In *International conference on machine learning*, pages 639–668, 2022.
- [4] Anish Athalye, Nicholas Carlini, and David Wagner. Obfuscated gradients give a false sense of security: Circumventing defenses to adversarial examples. In *International conference on machine learning*, pages 274–283, 2018.
- [5] Anish Athalye, Logan Engstrom, Andrew Ilyas, and Kevin Kwok. Synthesizing robust adversarial examples. In *International conference on machine learning*, pages 284–293, 2018.
- [6] Peter L Bartlett, Philip M Long, and Olivier Bousquet. The dynamics of sharpness-aware minimization: Bouncing across ravines and drifting towards wide minima. *Journal of Machine Learning Research*, 24(316):1–36, 2023.
- [7] Jeremy Bernstein and Laker Newhouse. Modular duality in deep learning. In *ICML*, 2025.
- [8] Léon Bottou. Stochastic gradient descent tricks. In *Neural networks: tricks of the trade: second edition*, pages 421–436. Springer, 2012.
- [9] Nicholas Carlini and David Wagner. Towards evaluating the robustness of neural networks. In *IEEE Symposium on Security and Privacy (S&P)*, pages 39–57, 2017.

- [10] Lizhang Chen, Jonathan Li, and Qiang Liu. Muon optimizes under spectral norm constraints. *arXiv preprint arXiv:2506.15054*, 2025.
- [11] Jeremy Cohen, Elan Rosenfeld, and Zico Kolter. Certified adversarial robustness via randomized smoothing. In *international conference on machine learning*, pages 1310–1320, 2019.
- [12] Francesco Croce, Maksym Andriushchenko, Vikash Sehwal, Edoardo Debenedetti, Nicolas Flammarion, Mung Chiang, Prateek Mittal, and Matthias Hein. Robustbench: a standardized adversarial robustness benchmark. In *Conference on Neural Information Processing Systems*, 2021.
- [13] Francesco Croce and Matthias Hein. Reliable evaluation of adversarial robustness with an ensemble of diverse parameter-free attacks. In *International conference on machine learning*, pages 2206–2216, 2020.
- [14] Francesco Croce and Matthias Hein. Adversarial robustness against multiple and single l_p -threat models via quick fine-tuning of robust classifiers. In *International Conference on Machine Learning*, pages 4436–4454, 2022.
- [15] Ali Dabouei, Fariborz Taherkhani, Sobhan Soleymani, and Nasser M Nasrabadi. Revisiting outer optimization in adversarial training. In *European Conference on Computer Vision*, pages 244–261, 2022.
- [16] Jia Deng, Wei Dong, Richard Socher, Li-Jia Li, Kai Li, and Li Fei-Fei. Imagenet: A large-scale hierarchical image database. In *2009 IEEE conference on computer vision and pattern recognition*, pages 248–255, 2009.
- [17] Zhun Deng, Hangfeng He, Jiaoyang Huang, and Weijie Su. Towards understanding the dynamics of the first-order adversaries. In *International Conference on Machine Learning*, pages 2484–2493, 2020.
- [18] Alexey Dosovitskiy, Lucas Beyer, Alexander Kolesnikov, Dirk Weissenborn, Xiaohua Zhai, Thomas Unterthiner, Mostafa Dehghani, Matthias Minderer, Georg Heigold, Sylvain Gelly, et al. An image is worth 16x16 words: Transformers for image recognition at scale. In *ICLR*, pages 1–13, 2021.
- [19] Alexey Dosovitskiy, Lucas Beyer, Alexander Kolesnikov, Dirk Weissenborn, Xiaohua Zhai, Thomas Unterthiner, Mostafa Dehghani, Matthias Minderer, Georg Heigold, Sylvain Gelly, Jakob Uszkoreit, and Neil Houlsby. An image is worth 16x16 words: Transformers for image recognition at scale. *ArXiv*.
- [20] Pierre Foret, Ariel Kleiner, Hossein Mobahi, and Behnam Neyshabur. Sharpness-aware minimization for efficiently improving generalization. In *ICLR*, 2021.
- [21] Ruiqi Gao, Tianle Cai, Haochuan Li, Cho-Jui Hsieh, Liwei Wang, and Jason D Lee. Convergence of adversarial training in overparametrized neural networks. *Advances in Neural Information Processing Systems*, 32, 2019.
- [22] Ian J Goodfellow, Jonathon Shlens, and Christian Szegedy. Explaining and harnessing adversarial examples. In *ICLR*, 2015.
- [23] Kaiming He, Xiangyu Zhang, Shaoqing Ren, and Jian Sun. Deep residual learning for image recognition. In *Proceedings of the IEEE conference on computer vision and pattern recognition*, pages 770–778, 2016.
- [24] Kaiming He, Xiangyu Zhang, Shaoqing Ren, and Jian Sun. Identity mappings in deep residual networks. In *European conference on computer vision*, pages 630–645. Springer, 2016.
- [25] Matthias Hein and Maksym Andriushchenko. Formal guarantees on the robustness of a classifier against adversarial manipulation. *Advances in neural information processing systems*, 30, 2017.
- [26] Nicholas J Higham. *Functions of matrices: theory and computation*. SIAM, 2008.

- [27] Daniel Jakubovitz and Raja Giryes. Improving dnn robustness to adversarial attacks using jacobian regularization. In *Proceedings of the European conference on computer vision (ECCV)*, pages 514–529, 2018.
- [28] Keller Jordan, Yuchen Jin, Vlado Boza, Jiacheng You, Franz Cesista, Laker Newhouse, and Jeremy Bernstein. Muon: An optimizer for hidden layers in neural networks. <https://kellerjordan.github.io/posts/muon/>, 2024.
- [29] Diederik P Kingma and Jimmy Ba. Adam: A method for stochastic optimization. In *ICLR*, 2015.
- [30] Alex Krizhevsky and Geoffrey Hinton. A learning multiple layers of features from tiny images. <http://www.cs.toronto.edu/~kriz/cifar.html>, 2009.
- [31] Jingyuan Liu, Jianlin Su, Xingcheng Yao, Zhejun Jiang, Guokun Lai, Yulun Du, Yidao Qin, Weixin Xu, Enzhe Lu, Junjie Yan, et al. Muon is scalable for llm training. *arXiv preprint arXiv:2502.16982*, 2025.
- [32] Liming Liu, Zhenghao Xu, Zixuan Zhang, Hao Kang, Zichong Li, Chen Liang, Weizhu Chen, and Tuo Zhao. Cosmos: A hybrid adaptive optimizer for memory-efficient training of llms. *arXiv preprint arXiv:2502.17410*, 2025.
- [33] Shengchao Liu, Dimitris Papailiopoulos, and Dimitris Achlioptas. Bad global minima exist and sgd can reach them. *Advances in Neural Information Processing Systems*, 33:8543–8552, 2020.
- [34] Ilya Loshchilov and Frank Hutter. Decoupled weight decay regularization. In *ICLR*, 2017.
- [35] Avery Ma, Yangchen Pan, and Amir-massoud Farahmand. Understanding the robustness difference between stochastic gradient descent and adaptive gradient methods. *Transactions on Machine Learning Research*, 2023.
- [36] Aleksander Madry, Aleksandar Makelov, Ludwig Schmidt, Dimitris Tsipras, and Adrian Vladu. Towards deep learning models resistant to adversarial attacks. In *ICLR*, 2018.
- [37] Laker Newhouse, R Preston Hess, Franz Cesista, Andrii Zahorodnii, Jeremy Bernstein, and Phillip Isola. Training transformers with enforced lipschitz constants. *arXiv preprint arXiv:2507.13338*, 2025.
- [38] Tianyu Pang, Kun Xu, Yinpeng Dong, Chao Du, Ning Chen, and Jun Zhu. Rethinking softmax cross-entropy loss for adversarial robustness. In *ICLR*, 2020.
- [39] Tianyu Pang, Xiao Yang, Yinpeng Dong, Hang Su, and Jun Zhu. Bag of tricks for adversarial training. In *ICLR*, 2021.
- [40] Herbert Robbins and Sutton Monro. A stochastic approximation method. *The annals of mathematical statistics*, pages 400–407, 1951.
- [41] Ali Shafahi, Mahyar Najibi, Mohammad Amin Ghiasi, Zheng Xu, John Dickerson, Christoph Studer, Larry S Davis, Gavin Taylor, and Tom Goldstein. Adversarial training for free! *Advances in neural information processing systems*, 32, 2019.
- [42] Wei Shen, Ruichuan Huang, Minhui Huang, Cong Shen, and Jiawei Zhang. On the convergence analysis of muon. *arXiv preprint arXiv:2505.23737*, 2025.
- [43] Christian Szegedy, Vincent Vanhoucke, Sergey Ioffe, Jon Shlens, and Zbigniew Wojna. Rethinking the inception architecture for computer vision. In *Proceedings of the IEEE conference on computer vision and pattern recognition*, pages 2818–2826, 2016.
- [44] Christian Szegedy, Wojciech Zaremba, Ilya Sutskever, Joan Bruna, Dumitru Erhan, Ian Goodfellow, and Rob Fergus. Intriguing properties of neural networks. In *ICLR*, 2014.
- [45] Florian Tramer, Nicholas Carlini, Wieland Brendel, and Aleksander Madry. On adaptive attacks to adversarial example defenses. *Advances in neural information processing systems*, 33:1633–1645, 2020.

- [46] Yusuke Tsuzuku, Issei Sato, and Masashi Sugiyama. Lipschitz-margin training: Scalable certification of perturbation invariance for deep neural networks. *Advances in neural information processing systems*, 31, 2018.
- [47] Yisen Wang, Xingjun Ma, James Bailey, Jinfeng Yi, Bowen Zhou, and Quanquan Gu. On the convergence and robustness of adversarial training. In *International Conference on Machine Learning*, pages 6586–6595, 2019.
- [48] Eric Wong, Leslie Rice, and J Zico Kolter. Fast is better than free: Revisiting adversarial training. In *ICLR*, 2020.
- [49] Dongxian Wu, Shu-Tao Xia, and Yisen Wang. Adversarial weight perturbation helps robust generalization. *Advances in neural information processing systems*, 33:2958–2969, 2020.
- [50] Weilin Xu, David Evans, and Yanjun Qi. Feature squeezing: Detecting adversarial examples in deep neural networks. In *Proceedings 2018 Network and Distributed System Security Symposium*, 2018.
- [51] Sergey Zagoruyko and Nikos Komodakis. Wide residual networks. In *British Machine Vision Conference*, pages 1–15, 2016.
- [52] Hongyang Zhang, Yaodong Yu, Jiantao Jiao, Eric Xing, Laurent El Ghaoui, and Michael Jordan. Theoretically principled trade-off between robustness and accuracy. In *International conference on machine learning*, pages 7472–7482, 2019.
- [53] Yihao Zhang, Hangzhou He, Jingyu Zhu, Huanran Chen, Yifei Wang, and Zeming Wei. On the duality between sharpness-aware minimization and adversarial training. In *International Conference on Machine Learning*, pages 59024–59041, 2024.
- [54] Zhanpeng Zhou, Mingze Wang, Yuchen Mao, Bingrui Li, and Junchi Yan. Sharpness-aware minimization efficiently selects flatter minima late in training. In *ICLR*, 2025.

Algorithm 2 One Muon Step under AT (expands line 10 of Alg. 1 when Opt = Muon; Newton–Schulz iteration inlined as sub-steps of S2).

Require: Weight block $W \in \mathbb{R}^{m \times n}$, momentum buffer M (init. $\mathbf{0}$), gradient $G = \nabla_W L_{\text{adv}}$, learning rate η , momentum μ , weight decay λ , Newton–Schulz steps s

- 1: **[S1]** $M \leftarrow \mu M + G$ \triangleright momentum update (Assumption 2.1: G is the β -smooth AT gradient)
- 2: **[S2]** // Approximate polar factor — supports **Lemma 2.1**
- 3: $X \leftarrow M / \|M\|_F$ \triangleright normalize, starts near Stiefel manifold
- 4: **for** $k = 1$ **to** s **do**
- 5: $X \leftarrow \frac{3}{2}X - \frac{1}{2}XX^\top X$ \triangleright Newton–Schulz polar iteration
- 6: **end for**
- 7: $\tilde{U} \leftarrow X$ \triangleright as in Theorem 2.1
- 8: **[S3]** $W \leftarrow (1 - \eta\lambda)W - \eta\tilde{U}$ \triangleright ; orthogonalised weight update (Theorem 2.1:
 $\|W_t\|_2 \leq \max(\|W_0\|_2, \frac{1+\varepsilon}{\lambda}), \text{ for all } t \geq 0)$
- 9: **return** updated W , updated M

A Related Work

Optimizer design is of significant importance in AT, which relies on the min-max optimization mechanism [36, 52]. These studies postulate that a stronger inner attack yields a more robust defense model. If the attack is too weak, it can lead to gradient masking or an overestimation of robustness.

Most theoretical research on AT focuses on the dynamics of min-max optimization, while less attention is paid to the choice of optimizer itself [47, 21, 17]. Early studies found that SGD optimization can lead to a more robust loss landscape when combined with regularization and data augmentation [33]. AT with the SGD optimizer and weight decay regularization can achieve feature purification [1]. Empirical studies have found it more suitable to apply SGD with momentum rather than other adaptive optimizers [39].

SAM minimizes both the loss value and its sharpness [20]. It can help improve the robustness of neural networks [53, 54]. The implicit bias of SAM yields a better generalization solution than that of standard gradient descent [3]. At the same time, SAM tends to “bounce” on both sides along the direction of maximum curvature; in more general cases, the effect of SAM is linked to the regularization of the Hessian spectrum (especially the maximum eigenvalue) [6]. However, SAM requires two forward-backward passes per step: one for the gradient perturbation and another for the actual update [20].

Previous studies have stated that SGD-trained neural networks provide better robustness to input perturbations than those trained with adaptive gradient methods due to smaller Lipschitz constants [35]. Recently, the Muon optimizer [28, 31] has been proposed in the training process of new foundation models. When the Hessian satisfies the low-rank property, Muon demonstrates a significant convergence speed advantage over SGD [42]. Using a Lyapunov function, it has been proven that Muon with momentum and decoupled weight decay is stable and converges to the KKT point of the implicitly constrained problem [10]. The Muon optimizer is built on Newton–Schulz iterative updates, and Bernstein et al. [7] constructed dual mappings for general network structures. This analytical framework can also be extended to the Muon optimizer. Newhouse et al. [37] proposed training a Transformer with Lipschitz constraints, employing constraint techniques such as Muon and soft cap. Although Chen et al. [10] analyze Muon’s convergence behavior under spectral norm constraints in a general nonconvex optimization setting, its effectiveness under AT has not been fully studied.

B Mapping of Theory and Algorithm

Algorithm 2 illustrates the inline mechanism of `Opt.step()` described in Algorithm 1.

Table 9 maps theoretical results with algorithmic operations of the Newton–Schulz sub-routine defined in Algorithm 2.

Table 9: Mapping of algorithmic operations and theoretical results.

Step	Operation	Theory	Implication
S1	$M \leftarrow \mu M + G$	Assumption 2.1	β -smooth adversarial loss
S2 (init)	$X \leftarrow M/\ M\ _F$	Lemma 2.1 (pre-cond.)	Normalizes scales
S2 (loop)	$X \leftarrow \frac{3}{2}X - \frac{1}{2}XX^\top X$	Theorem 2.1 (Newton–Schulz approximation and tolerance condition)	$\ \tilde{U}\ _2 \approx 1$
S3	$W \leftarrow (1-\eta\lambda)W - \eta\tilde{U}$	Theorem 2.1	Bounded $\ W_t\ _2$ trajectory
S3 (all layers)	Multi-norm Δ_{union}	Theorem 2.2	Union robustness analysis
S3	AT loss descent	Theorem 2.3	Nuclear-norm descent $\ M\ _*$

C Supplementary Theoretical Remarks

Remark C.1 (Interpretation of Proposition 2.1). We acknowledge that true adversarial robustness depends on the global geometry of the model’s decision boundary, not merely on local gradient magnitudes. The first-order characterization adopted here reveals robustness to the dual norm of the input gradient. It is a standard proxy used throughout the certification literature [25, 46]. It is exact for linear models and provides a tight bound in locally linear regions of ReLU networks. Although it does not capture higher-order curvature effects (e.g., decision boundary curvature exploited by second-order attacks), it remains predictive in practice.

Remark C.2 (Interpretation of Proposition 2.2). For residual architectures, Proposition 2.2 can be applied blockwise. A block $h_{\ell+1} = h_\ell + F_\ell(h_\ell)$ satisfies $\|Jh_{\ell+1}\|_2 \leq 1 + \|JF_\ell(h_\ell)\|_2$, and hence the network Jacobian is bounded by the product of such residual-block factors. Therefore, the sequential feedforward bound is used as a clean base case, while ResNet/WRN-style architectures follow by replacing each layer factor with its corresponding residual-block Lipschitz factor.

Remark C.3 (Interpretation of Theorem 2.1). Theorem 2.1 says that Muon’s polar update admits a spectral-norm stability ceiling: the weight decay term $\eta\lambda$ pulls the spectral norm toward zero, while the orthonormalized update adds at most $\eta(1 + \bar{\varepsilon})$ per step. These two forces balance at the fixed point $\|W\|_2 = (1 + \bar{\varepsilon})/\lambda$, giving a hard ceiling that depends only on the learning rate, weight decay, and approximation quality of Newton–Schulz iterations. Theorem 2.1 is a worst-case stability bound on the trajectory induced by bounded operator-norm updates. It should not be read as predicting that Muon yields smaller empirical weight spectral norms than SGD. In practice, SGD can yield even smaller spectral norms under AT. The theoretical content is that Muon’s polar update cannot induce unbounded spectral growth. It is a property that distinguishes it from adaptive optimizers like AdamW, where we empirically observe such growth. The bound is therefore read as a sufficient condition for spectral stability. This theorem asserts that the polar update guarantees $\|W_t\|_2 \leq \max(\|W_0\|_2, (1 + \bar{\varepsilon})/\lambda)$, preventing unbounded spectral growth. This theorem does not claim the bound is tight.

Remark C.4 (Interpretation of Theorem 2.2). The quantity $\hat{L}_p(\theta)$ is a computable upper bound on the true ℓ_p -Lipschitz constant $L_p(\theta)$, obtained by chaining (i) the Jacobian–spectral bound of Proposition 2.2, (ii) the per-layer spectral bound $\|W_\ell\|_2 \leq B_\ell$ from Theorem 2.1, and (iii) the norm-equivalence $\|\delta\|_2 \leq c_p\|\delta\|_p$. Theorem 2.2 should be read as a structural statement rather than a usable robustness certificate. Specifically, it reflects that Muon’s polar update in the context of empirical defense prevents unbounded spectral (hence Lipschitz) growth along the trajectory.

Remark C.5 (Interpretation of Theorem 2.3). Theorem 2.3 shows that Muon’s update provides a descent guarantee in the robust min-max optimization setting. Since the nuclear norm $\|M\|_* = \sum_i \sigma_i(M)$ accumulates all singular values of the gradient, the guaranteed descent is structurally larger than that of a raw gradient step, while the rank-bounded curvature term prevents the oscillations commonly observed with SGD under the high-variance adversarial loss landscape. In practice, Muon consistently achieves lower loss earlier and with less oscillation than other optimizers like SGD and AdamW across all architectures and norm settings, with the effect being most pronounced on ViT, where polar orthogonalization more effectively controls the rank structure of attention weight gradients.

D Proof of Theoretical Analysis

D.1 Proof of Lemma 2.1

Proof. Let $U = \text{Ortho}(A) = PV^\top$, where $A = P\Sigma V^\top$ is the compact SVD of A . If $m \geq n$, then $P^\top P = I_n$ and V is orthogonal. Hence

$$U^\top U = VP^\top PV^\top = I_n.$$

Moreover, since $A^\top A = V\Sigma^2 V^\top$, we have

$$U(A^\top A)^{1/2} = PV^\top(V\Sigma V^\top) = P\Sigma V^\top = A.$$

If $m < n$, then P is orthogonal and $V^\top V = I_m$. Hence

$$UU^\top = PV^\top VP^\top = I_m.$$

Moreover, since $AA^\top = P\Sigma^2 P^\top$, we have

$$(AA^\top)^{1/2}U = (P\Sigma P^\top)(PV^\top) = P\Sigma V^\top = A.$$

Thus, all nonzero singular values of U are equal to one, and therefore $\|U\|_2 = 1$.

It remains to prove the projection statement. Let \mathcal{S} denote the corresponding rectangular Stiefel set, i.e., $\mathcal{S} = \{Q : Q^\top Q = I_n\}$ if $m \geq n$, and $\mathcal{S} = \{Q : QQ^\top = I_m\}$ if $m < n$. For any $Q \in \mathcal{S}$,

$$\|A - Q\|_F^2 = \|A\|_F^2 + \|Q\|_F^2 - 2\langle A, Q \rangle.$$

Since $\|Q\|_F^2 = \min\{m, n\}$ is fixed on \mathcal{S} , minimizing $\|A - Q\|_F$ is equivalent to maximizing $\langle A, Q \rangle$. By von Neumann's trace inequality,

$$\langle A, Q \rangle \leq \sum_i \sigma_i(A)\sigma_i(Q) = \sum_i \sigma_i(A),$$

because every $Q \in \mathcal{S}$ has all nonzero singular values equal to one. For $Q = U = PV^\top$, equality holds:

$$\langle A, U \rangle = \text{tr}(A^\top U) = \text{tr}(\Sigma) = \sum_i \sigma_i(A).$$

Hence U is a minimizer of $\min_{Q \in \mathcal{S}} \|A - Q\|_F$. The proof is complete. \square

D.2 Proof of Theorem 2.1

Proof. Using the triangle inequality and absolute homogeneity of the spectral norm, we have

$$\|W_{t+1}\|_2 = \left\| (1 - \eta\lambda)W_t - \eta\tilde{U}_t \right\|_2 \leq (1 - \eta\lambda)\|W_t\|_2 + \eta\|\tilde{U}_t\|_2. \quad (15)$$

Applying the assumption of Eq. (6) with $a_t = \|W_t\|_2$, we obtain

$$a_{t+1} \leq (1 - \eta\lambda)a_t + \eta + \eta\varepsilon_t. \quad (16)$$

Unrolling the recursion gives

$$a_t \leq (1 - \eta\lambda)^t a_0 + \eta \sum_{k=0}^{t-1} (1 - \eta\lambda)^{t-1-k} + \eta \sum_{k=0}^{t-1} (1 - \eta\lambda)^{t-1-k} \varepsilon_k. \quad (17)$$

The second term is a geometric series

$$\eta \sum_{k=0}^{t-1} (1 - \eta\lambda)^{t-1-k} = \eta \sum_{j=0}^{t-1} (1 - \eta\lambda)^j = \eta \cdot \frac{1 - (1 - \eta\lambda)^t}{\eta\lambda} = \frac{1 - (1 - \eta\lambda)^t}{\lambda}. \quad (18)$$

Substituting back yields Eq. (8). If $\varepsilon_k \leq \bar{\varepsilon}$, then

$$\eta \sum_{k=0}^{t-1} (1 - \eta\lambda)^{t-1-k} \varepsilon_k \leq \eta \bar{\varepsilon} \sum_{j=0}^{t-1} (1 - \eta\lambda)^j = \bar{\varepsilon} \cdot \frac{1 - (1 - \eta\lambda)^t}{\lambda}, \quad (19)$$

which gives Eq. (9). The proof is complete. \square

D.3 Proof of Theorem 2.2

Proof. Step 1: From Jacobian spectral norms to an ℓ_2 -Lipschitz bound on the margin.

For each competing class $j \neq y$, define the pairwise margin

$$m_{y,j}(x) := g_\theta(x)_y - g_\theta(x)_j = \langle e_y - e_j, g_\theta(x) \rangle. \quad (20)$$

Here $e_y - e_j$ is fixed and satisfies $\|e_y - e_j\|_2 = \sqrt{2}$. Hence

$$\nabla_x m_{y,j}(x) = J_{g_\theta}(x)^\top (e_y - e_j), \quad (21)$$

and therefore, it satisfies

$$\|\nabla_x m_{y,j}(x)\|_2 \leq \sqrt{2} \|J_{g_\theta}(x)\|_2 \leq \sqrt{2} \prod_{\ell=1}^L \|W_\ell\|_2, \quad (22)$$

where the last inequality follows from Proposition 2.2 assuming 1-Lipschitz activations. Otherwise, the product is replaced by $L_\phi^{L-1} \prod_{\ell=1}^L \|W_\ell\|_2$.

Since the multiclass margin can be written as

$$m_\theta(x, y) = g_\theta(x)_y - \max_{j \neq y} g_\theta(x)_j = \min_{j \neq y} m_{y,j}(x), \quad (23)$$

and the pointwise minimum of finitely many L -Lipschitz functions is still L -Lipschitz, $m_\theta(\cdot, y)$ is $L_2(\theta)$ -Lipschitz with respect to $\|\cdot\|_2$, with

$$L_2(\theta) \leq C_{\text{marg}} \prod_{\ell=1}^L \|W_\ell\|_2, \quad C_{\text{marg}} := \max_{j \neq y} \|e_y - e_j\|_2 = \sqrt{2}. \quad (24)$$

Step 2: Spectral-norm control from Muon.

By Theorem 2.1, running Muon with learning rate η and weight decay $\lambda > 0$ guarantees

$$\|W_\ell\|_2 \leq B_\ell \quad \text{for all } \ell \in \{1, \dots, L\} \text{ and all training steps,} \quad (25)$$

where $B_\ell = \max(\|W_\ell^{(0)}\|_2, (1 + \bar{\varepsilon})/\lambda)$. Combining with Eq. (24) yields

$$L_2(\theta) \leq C_{\text{marg}} \prod_{\ell=1}^L B_\ell. \quad (26)$$

Step 3: From ℓ_2 -Lipschitzness to ℓ_p -Lipschitzness via norm equivalence.

For each $p \in \{1, 2, \infty\}$, let c_p denote the norm-equivalence constant satisfying

$$\|\delta\|_2 \leq c_p \|\delta\|_p, \quad \text{for all } \delta \in \mathbb{R}^d, \quad (27)$$

with $c_\infty = \sqrt{d}$, $c_2 = 1$, and $c_1 = 1$. Then for any $\delta \in \mathbb{R}^d$ and any $p \in \mathcal{P}$,

$$|m_\theta(x + \delta, y) - m_\theta(x, y)| \leq L_2(\theta) \|\delta\|_2 \leq L_2(\theta) c_p \|\delta\|_p \leq \hat{L}_p(\theta) \|\delta\|_p, \quad (28)$$

where

$$\hat{L}_p(\theta) := c_p C_{\text{marg}} \prod_{\ell=1}^L B_\ell$$

is the computable upper bound from Eq. (10), and the last inequality uses Eq. (26).

Step 4: Union robustness.

Take any $\delta \in \Delta_{\text{union}} = \bigcup_{p \in \mathcal{P}} \{\delta : \|\delta\|_p \leq \varepsilon_p\}$. Then there exists some $p \in \mathcal{P}$ with $\|\delta\|_p \leq \varepsilon_p$. By (28),

$$m_\theta(x + \delta, y) \geq m_\theta(x, y) - \hat{L}_p(\theta) \|\delta\|_p \geq m_\theta(x, y) - \hat{L}_p(\theta) \varepsilon_p \geq m_\theta(x, y) - \max_{p' \in \mathcal{P}} \hat{L}_{p'}(\theta) \varepsilon_{p'}. \quad (29)$$

Under the assumption of Theorem 2.2, $m_\theta(x, y) > \max_{p' \in \mathcal{P}} \hat{L}_{p'}(\theta) \varepsilon_{p'}$, hence $m_\theta(x + \delta, y) > 0$. Since $\delta \in \Delta_{\text{union}}$ was arbitrary, $m_\theta(x + \delta, y) > 0$ for all $\delta \in \Delta_{\text{union}}$. Thus, the claim follows. \square

D.4 Proof of Theorem 2.3

Proof. Let M denote the momentum-accumulated gradient used by Muon, and let \tilde{U} denote the inexact Newton–Schulz output satisfying

$$\|\tilde{U} - \text{Ortho}(M)\|_F \leq \delta_{\text{orth}}, \quad \|\tilde{U}\|_2 \leq 1 + \varepsilon, \quad \|\tilde{U}\|_F^2 \leq r(1 + \varepsilon)^2, \quad (30)$$

where $r = \text{rank}(M)$, or any upper bound on it. Consider the actual update $W^+ = W - \eta \tilde{U}$. By Assumption 2.1 (β -smoothness of F w.r.t. $\|\cdot\|_F$), we have

$$F(W^+) \leq F(W) - \eta \langle G, \tilde{U} \rangle + \frac{\beta}{2} \eta^2 \|\tilde{U}\|_F^2. \quad (31)$$

We decompose the inner product as

$$\langle G, \tilde{U} \rangle = \underbrace{\langle M, \text{Ortho}(M) \rangle}_{\text{(i)}} + \underbrace{\langle G - M, \tilde{U} \rangle}_{\text{(ii)}} + \underbrace{\langle M, \tilde{U} - \text{Ortho}(M) \rangle}_{\text{(iii)}}. \quad (32)$$

(i) Ideal inner-product term. By the same SVD argument as in the idealized case (Lemma 2.1), the polar factor satisfies

$$\langle M, \text{Ortho}(M) \rangle = \|M\|_*, \quad (33)$$

where $\|M\|_* = \sum_{i=1}^r \sigma_i(M)$ is the nuclear norm.

(ii) Gradient–momentum mismatch. By Hölder’s inequality for Schatten norms, i.e., the duality between the nuclear norm and the spectral norm, we have

$$\langle G - M, \tilde{U} \rangle \geq -\|G - M\|_* \|\tilde{U}\|_2 \geq -(1 + \varepsilon) \|G - M\|_*. \quad (34)$$

(iii) Orthogonalization error. By the Cauchy–Schwarz inequality for the Frobenius inner product,

$$\begin{aligned} |\langle M, \tilde{U} - \text{Ortho}(M) \rangle| &\leq \|M\|_F \|\tilde{U} - \text{Ortho}(M)\|_F \\ &\leq \|M\|_F \delta_{\text{orth}} \\ &\leq \sqrt{r} \|M\|_2 \delta_{\text{orth}}, \end{aligned} \quad (35)$$

where the last step uses $\|M\|_F \leq \sqrt{r} \|M\|_2$.

Combining (i)–(iii). Substituting Eq. (33), Eq. (34), and Eq. (35) into Eq. (32) gives

$$\langle G, \tilde{U} \rangle \geq \|M\|_* - (1 + \varepsilon) \|G - M\|_* - \sqrt{r} \|M\|_2 \delta_{\text{orth}}. \quad (36)$$

Plugging Eq. (36) into (31) and using $\|\tilde{U}\|_F^2 \leq r(1 + \varepsilon)^2$, we obtain

$$\begin{aligned} F(W^+) &\leq F(W) - \eta \|M\|_* + \eta(1 + \varepsilon) \|G - M\|_* \\ &\quad + \eta \sqrt{r} \|M\|_2 \delta_{\text{orth}} + \frac{\beta}{2} \eta^2 r(1 + \varepsilon)^2. \end{aligned} \quad (37)$$

This is exactly the descent inequality of Theorem 2.3. The proof is complete. \square

E Spectral Analysis: Spectral Norms and Condition Numbers

As a lightweight diagnostic of the optimization-side mechanism of Muon on spectral conditioning and robustness, we track the mean per-layer condition number $\kappa = \sigma_{\max}/\sigma_{\min}$ every 5 epochs throughout AT on PreActResNet-18 (Figure 2). Muon maintains a low and stable $\kappa \approx 5$ throughout training, comparable to SGD, while AdamW’s κ grows rapidly to ≈ 50 within the first 30 epochs. Correlating κ with robust accuracy (Figure 3) reveals two distinct regimes: SGD and Muon concentrate in the low κ , high-robustness region, while AdamW occupies the high κ , lower-robustness region. This phenomenon suggests that what determines robustness may not be purely “Jacobian scale”, but rather “Jacobian geometry”, that is, whether the distribution of singular values is balanced. This supports the interpretation that spectral conditioning acts as a *regularizer for the optimization dynamics* of AT. A well-conditioned weight matrix propagates gradients more uniformly during backpropagation, mitigating the vanishing/exploding gradient issues that otherwise destabilize AT.

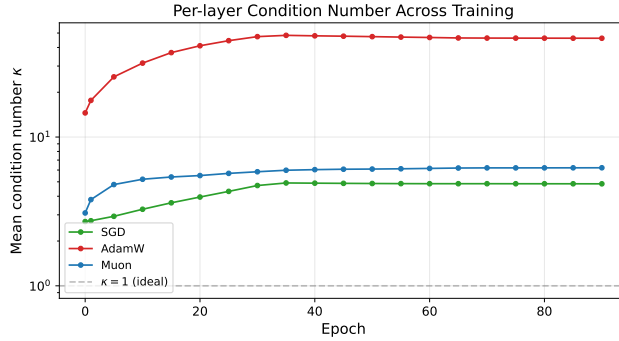


Figure 2: Per-layer condition number change during training.

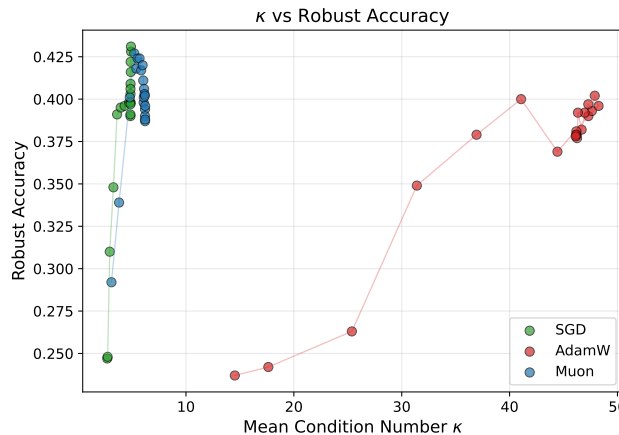


Figure 3: Spectral conditioning and robustness.

These diagnostics show that SGD often achieves the smallest absolute spectral norm, consistent with its strong robustness under AT. Muon does not uniformly dominate SGD in terms of raw spectral-norm magnitude. Instead, its spectral behavior is consistently closer to SGD than to AdamW, and it avoids the large spectral growth observed for AdamW in several settings. Therefore, our claim should be interpreted as the stability ceiling rather than the strict minimization of weight spectral norms. This also explains why SGD remains a very strong baseline, while Muon provides a more stable alternative to AdamW.

To probe the empirical tightness of the spectral-norm bound, we train PreActResNet-18, WRN-34-10, and ViT-B for 100 epochs on CIFAR-10 using the multi-norm $\ell_\infty + \ell_1$ pipeline (APGD-10 attack, piecewise LR schedule, $\lambda = 5 \times 10^{-4}$). Fig. 4 shows per-epoch median and max $\|W_\ell\|_2$ trajectories under each optimizer. Three observations support Theorem 2.1’s interpretation as a stability distinction rather than a tight bound. First, the ceiling holds universally with substantial slack. Across all 9 (model, optimizer) combinations, max $\|W_\ell\|_2$ stays within a single decade (around 1–55), three to four orders of magnitude below the theoretical ceiling $B = (1 + \bar{\epsilon})/\lambda \approx 2200$. The bound is loose by design: it certifies that Muon’s polar updates cannot induce unbounded spectral growth, not that $\|W_\ell\|_2$ approaches B . Second, Muon and SGD plateau by epoch 35 on every architecture. Both optimizers exhibit the LR-schedule-driven plateau predicted by Theorem 2.1 that spectral norms grow during the high-LR phase and stabilize once η is decayed at epoch 33. The plateau is architecture-invariant in qualitative shape, though absolute values differ across model sizes. Third, AdamW’s spectral behavior is regime-dependent. AdamW achieves the smallest spectral norms on PreActResNet-18, but the largest on WRN-34-10 and ViT-B. This non-monotonicity reflects the per-parameter scaling mechanism of AdamW: the update magnitude is governed by $m_t/(\sqrt{v_t} + \epsilon_{\text{AdamW}})$, where v_t is the gradient second-moment Exponential Moving Average (EMA). When the model is not large (PreActResNet-18), gradient directions are repetitive and v_t saturates rapidly, making AdamW behave as approximately constant-step SGD with bounded updates. When

the model is large enough that gradient statistics become heterogeneous across layers and directions (WRN-34-10), some directions develop near-zero v_t , amplifying the effective update without bound.

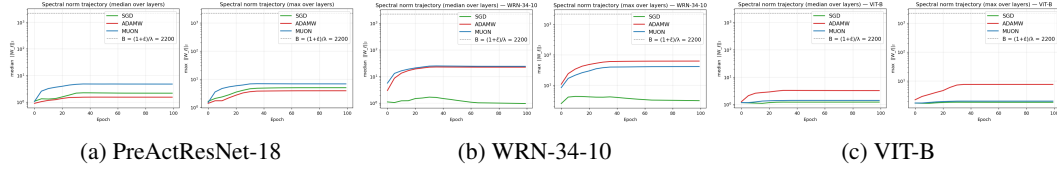


Figure 4: The spectral norm change with different optimizers during AT.

F Loss of Different Optimizers

Figures 5, 6, 7, 8, and 9 depict the training loss curves during AT on CIFAR-10 [30] with different optimizers on PreActResNet-18 [24], WRN-34-10 [51], WRN-34-20 [51], ViT-B [18], and ViT-L [18]. Across architectures, Muon converges faster and yields a smoother training-loss curve than both SGD and AdamW. These empirical observations are consistent with the nuclear-norm descent guarantee in Theorem 2.3. In contrast, on the ViT architecture [18], it is difficult to use an adaptive optimizer such as AdamW for AT. When AdamW exhibits numerical instability on ViTs, we report the resulting evaluation accuracies in the main tables rather than marking the runs as “failed”. Such cases are described as severe degradation or near-random performance when the reported robust accuracies are close to chance level.

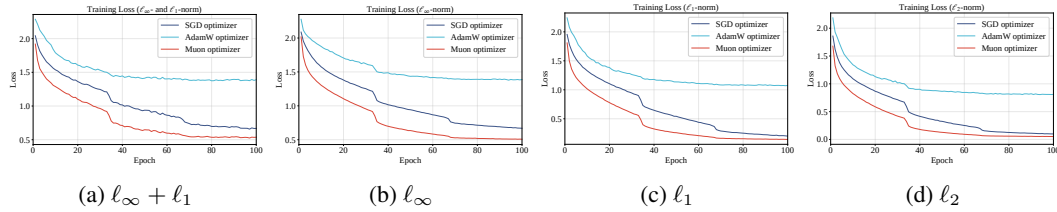


Figure 5: Training loss on PreActResNet-18 [24].

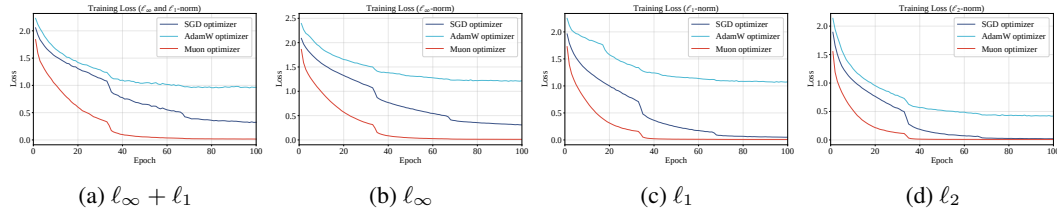


Figure 6: Training loss on WRN-34-10 [51].

Under controlled conditions (identical learning rate of 0.01 for all optimizers on PreActResNet-18), Figure 10 reveals a striking pattern: SGD produces the largest gradient norms, yet Muon achieves the fastest loss descent. This diagnostic suggests that Muon can descend the adversarial objective faster under the same nominal learning rate. However, because different optimizers induce different effective update magnitudes, this experiment should not be interpreted as isolating the update direction alone. Theorem 2.3 explains this: the polar factor $\text{Ortho}(M)$ maximizes the inner product $\langle G, U \rangle$ among all directions U with unit-norm columns, so each Muon step extracts the maximum possible descent per unit of parameter change. In contrast, SGD applies the raw gradient direction, which may not be well-conditioned and waste update magnitude on non-descent directions.

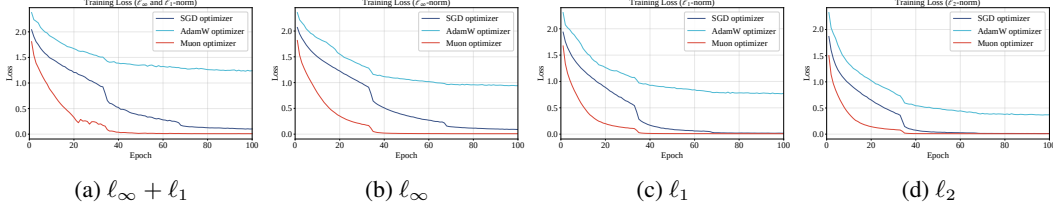


Figure 7: Training loss on WRN-34-20 [51].

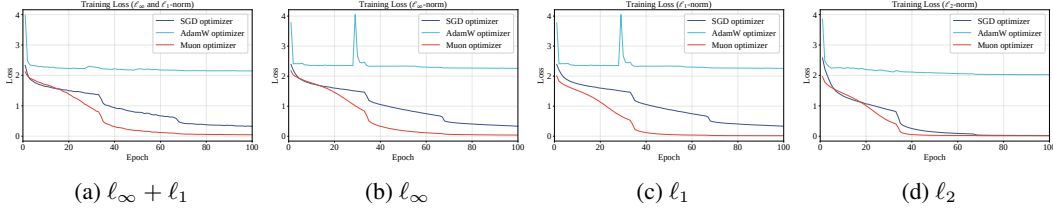


Figure 8: Training loss on ViT-B [18].

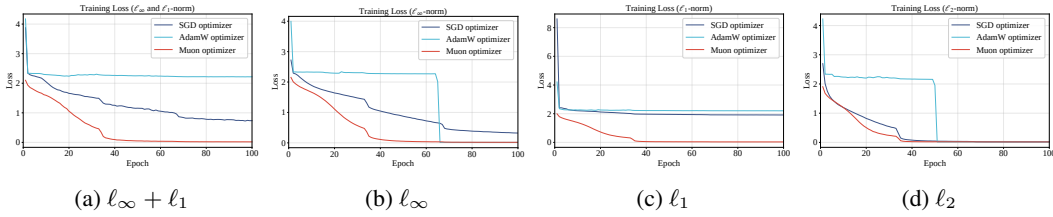


Figure 9: Training loss on ViT-L [18].

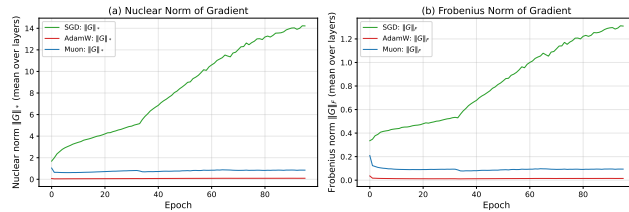


Figure 10: The variation tendency of nuclear gradient descent norms.

G Robust Overfitting Diagnostics

The “robust overfitting” phenomenon is a concern in adversarial learning. We visualize the clean accuracy, ℓ_∞ robust accuracy, and union robust accuracy of PreActResNet-18 [24]. On CIFAR-10, Figure 11 illustrates the transition process. As shown in the figures, Muon converges substantially faster than both SGD and AdamW in the early training phase: by epoch 10–15, Muon already achieves about 40–44% union robust accuracy, while SGD is still around 25–35% and AdamW around 30–38%. This rapid early convergence is consistent with our theoretical finding (Theorem 2.3) that Muon descends the adversarial loss along the gradient nuclear-norm direction, providing stronger per-step progress than vanilla SGD. From a practical standpoint, this means Muon can reach SGD-level robustness in roughly one-third of the training budget, which is a meaningful advantage in compute-constrained settings. In the later phase (epoch 40–100), Muon stabilizes at approximately 40% (ℓ_∞) and 40% (union), SGD converges to a similar level (about 40%), while AdamW continues to improve and ultimately reaches about 36%. The fact that AdamW gradually narrows the gap in the long run is an interesting finding. AdamW’s per-parameter adaptive scaling may contribute to this phenomenon. This trade-off between Muon (fast convergence and stable plateau) and AdamW (slow start but higher asymptote) is itself a novel empirical observation about optimizer dynamics under AT. We also note that the oscillation magnitude of SGD (green curve) in the first 35 epochs

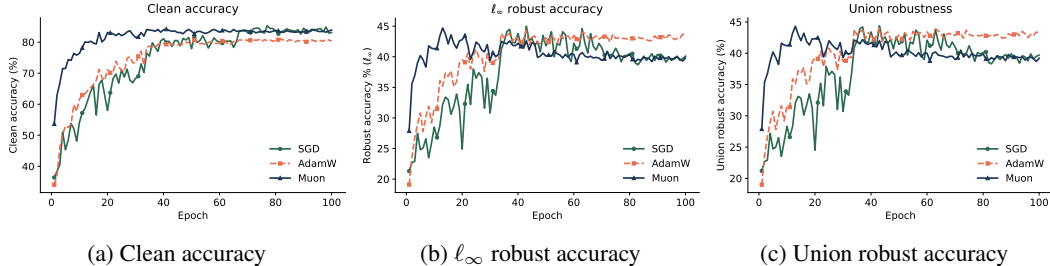


Figure 11: Robustness evaluation during AT process.

is substantially larger than Muon’s, which supports the paper’s claim about Muon providing more stable optimization geometry. This stability, combined with fast early convergence, makes Muon particularly attractive for architectures or settings where training is terminated early or computational budgets are tight.

In the main text, we have observed the same “robust overfitting” phenomenon in several Muon-based AT runs. In particular, the best checkpoint can achieve strong union robustness, whereas the last checkpoint may show a large degradation under the union attack. This indicates that Muon’s orthogonalized update geometry improves early and middle-stage robust optimization, but does not by itself eliminate late-stage robust overfitting. This observation refines our interpretation of Muon. The nuclear-norm descent view in Theorem 2.3 explains why Muon can make rapid early progress on the adversarial objective. However, robust overfitting also depends on learning-rate decay, momentum accumulation, finite-sample effects, and the mismatch between the sampled training threat norm and the full union evaluation. Therefore, Muon should be regarded as an optimizer-level mechanism that can accelerate robust optimization, rather than as a standalone robust-overfitting mitigation.

For practical use, we recommend robust-validation-based early stopping. Specifically, for multi-norm AT, checkpoints should be selected according to validation union robust accuracy rather than clean accuracy, final-epoch performance, or a single-norm robust metric. This criterion introduces no additional training cost and directly targets the evaluation metric of interest. Other alleviation methods, such as Adversarial Weight Perturbation (AWP) [49] and label smoothing [43], are complementary to Muon and can be combined with its orthogonalized update geometry in future work.

H Additional Empirical Robustness Experiments

H.1 AutoAttack Evaluation

We dive into further studies on empirical robustness to explore additional insights. Although APGD is used as the default evaluation attack for controlled optimizer comparisons, we further conduct stronger evaluations to rule out attack underfitting. Table 10 compares the defense methods [14] on three optimizers with some representative baseline methods, such as AT [36], FastAT [48] and its variant [2], FreeAT [41], and a defense built on Softmax Cross-Entropy Loss [38]. The evaluated model is WRN-34-10 [51]. It reports AutoAttack evaluation results under the RobustBench protocol with the threat model ℓ_∞ ($\epsilon = 8/255$). The Muon variant achieves 46.71% robust accuracy under AutoAttack [13], compared with 44.11% for SGD and 42.47% for AdamW.

H.2 Robustness under Stronger White-box Attacks

To rule out attack underfitting and loss-specific overestimation, we evaluate the trained models using stronger white-box attacks, including PGD-100 and CW-100 under both ℓ_∞ and ℓ_2 threat models. These evaluations complement AutoAttack/RobustBench-style testing and provide additional evidence that the observed robustness is not an artifact of the default APGD evaluation. Since Muon affects only the optimization trajectory during training, the deployed classifier remains a standard deterministic differentiable model. Hence, there is no inference-time stochastic transformation over which EOT must average, and no non-differentiable or gradient-obfuscating module for BPDA to approximate [4, 5]. This distinguishes our setting from preprocessing defense [50] or randomization methods [11], where adaptive attacks must be tailored to the defense mechanism [45]. We

Table 10: The robustness comparison (RobustBench [12]).

Method	Clean (%)	AutoAttack (%)
Defense [14] + Muon	83.16	46.71
Defense [14] + SGD	80.02	44.11
Defense [14] + AdamW	69.92	42.47
AT [36]	87.14	44.04
FastAT’s variant [2]	79.84	43.93
Softmax Cross-Entropy Loss [38]	80.89	43.48
FastAT [48]	83.34	43.21
FreeAT [41]	86.11	41.47

Table 11: The white-box attack evaluation results on PreActResNet-18 [24].

Norm	Opt.	Best				Last			
		PGD (ℓ_∞)	C&W (ℓ_∞)	PGD (ℓ_2)	C&W (ℓ_2)	PGD (ℓ_∞)	C&W (ℓ_∞)	PGD (ℓ_2)	C&W (ℓ_2)
$\ell_\infty + \ell_1$	SGD	43.44	43.25	66.29	65.32	37.30	38.23	64.96	64.67
	AdamW	39.24	39.55	56.56	55.67	24.74	24.89	57.87	56.12
	Muon	42.76	42.10	65.25	63.56	39.97	40.89	68.09	67.78
ℓ_∞	SGD	48.07	48.11	60.00	59.19	43.78	44.19	58.54	58.44
	AdamW	41.76	40.95	49.55	48.53	36.70	35.48	51.64	50.15
	Muon	47.03	45.66	61.15	59.19	45.12	45.78	62.07	61.97
ℓ_1	SGD	19.02	19.51	59.44	59.95	19.11	19.62	59.53	60.01
	AdamW	24.28	26.39	55.62	55.19	42.27	40.65	56.04	55.82
	Muon	25.97	27.03	59.39	58.32	19.76	20.81	63.67	64.23
ℓ_2	SGD	27.15	28.94	65.95	66.32	21.27	23.46	63.58	64.02
	AdamW	25.99	28.48	59.71	59.97	24.84	27.62	59.82	60.38
	Muon	29.88	31.71	65.23	64.75	25.12	25.80	67.06	67.40

therefore evaluate the resulting deterministic models using strong white-box attacks and AutoAttack protocols [13].

Table 11 checks the stronger white-box attack evaluation results on PreActResNet-18 [24]. The perturbation budgets are set to $\epsilon_\infty = 8/255$ and $\epsilon_2 = 0.5$ for ℓ_∞ and ℓ_2 attacks, respectively. For each norm, SGD, AdamW, and Muon are compared using best and last checkpoints across PGD-100 [36] and C&W-100 [9] attacks under ℓ_∞ and ℓ_2 settings. Overall, Muon achieves the robust performance in most groups, especially for the last checkpoint, indicating the applicability in the security-sensitive setting.

Table 12 reports white-box robustness on WRN-34-10 [51] under PGD-100 and C&W-100 attacks for both ℓ_∞ and ℓ_2 threat models. Across four training norms, Muon consistently delivers the strongest or near-strongest robustness, particularly at the last checkpoint. The gains are most pronounced under ℓ_1 and ℓ_2 training, suggesting that Muon is beneficial for robust generalization.

Table 13 presents white-box robustness results on WRN-34-20 [51] under PGD and C&W attacks with ℓ_∞ and ℓ_2 constraints. Across all training norms, Muon achieves the best or comparable robustness performance, with especially strong gains under ℓ_2 training. Its last-checkpoint results remain consistently competitive, suggesting improved robustness stability compared with SGD and AdamW.

H.3 Robustness under Black-box Attacks

Black-box transfer attacks provide a practical measure of robustness beyond model-specific white-box optimization. In realistic deployments, attackers may not know the exact architecture, parameters, or defense pipeline, but can still craft adversarial examples on surrogate models and transfer them to the target. Therefore, evaluating black-box adversarial examples tests whether robustness generalizes across attack sources rather than merely resisting a known gradient path. Strong black-box perfor-

Table 12: The white-box attack evaluation results on WRN-34-10 [51].

Norm	Opt.	Best				Last			
		PGD (ℓ_∞)	C&W (ℓ_∞)	PGD (ℓ_2)	C&W (ℓ_2)	PGD (ℓ_∞)	C&W (ℓ_∞)	PGD (ℓ_2)	C&W (ℓ_2)
$\ell_\infty + \ell_1$	SGD	40.48	40.60	64.59	63.73	33.30	33.89	61.91	61.98
	AdamW	39.47	40.64	61.38	61.05	37.89	39.02	62.80	62.44
	Muon	41.98	41.14	60.19	58.93	39.43	39.69	65.35	65.48
ℓ_∞	SGD	46.53	46.35	59.66	58.65	38.68	39.34	54.03	54.25
	AdamW	44.56	43.93	51.65	50.63	44.21	43.92	50.87	49.89
	Muon	49.41	48.80	60.48	59.53	44.81	45.05	54.72	55.12
ℓ_1	SGD	22.24	21.26	38.47	37.33	18.85	18.89	58.27	58.55
	AdamW	25.42	26.10	52.07	51.42	23.29	26.12	56.51	56.57
	Muon	27.20	28.89	60.53	59.87	22.50	22.77	63.32	63.48
ℓ_2	SGD	24.10	25.48	55.21	54.72	23.47	23.44	62.58	62.77
	AdamW	25.54	27.19	53.40	53.03	23.75	25.18	61.53	62.36
	Muon	28.77	28.96	68.33	68.59	28.85	29.04	68.76	68.99

Table 13: The white-box attack evaluation results on WRN-34-20 [51].

Norm	Opt.	Best				Last			
		PGD (ℓ_∞)	C&W (ℓ_∞)	PGD (ℓ_2)	C&W (ℓ_2)	PGD (ℓ_∞)	C&W (ℓ_∞)	PGD (ℓ_2)	C&W (ℓ_2)
$\ell_\infty + \ell_1$	SGD	40.58	39.12	62.14	60.47	35.23	35.53	62.25	62.42
	AdamW	38.34	37.86	59.50	58.12	38.34	37.86	59.49	58.12
	Muon	43.03	42.41	63.19	61.66	41.78	42.07	62.82	62.96
ℓ_∞	SGD	45.13	43.08	57.92	55.81	40.13	40.47	54.90	55.36
	AdamW	44.81	45.05	50.96	50.22	44.17	43.17	50.60	49.25
	Muon	49.71	48.56	60.39	59.07	47.71	48.01	57.83	58.08
ℓ_1	SGD	23.91	23.80	43.44	42.51	20.04	20.20	60.65	60.79
	AdamW	23.79	26.23	53.03	52.74	21.26	22.64	57.92	59.11
	Muon	24.20	24.43	65.88	66.05	23.65	23.74	65.36	65.44
ℓ_2	SGD	26.23	26.38	64.42	64.66	25.67	25.78	65.06	65.22
	AdamW	26.83	26.58	61.62	62.95	27.53	26.52	61.33	62.56
	Muon	30.71	30.88	70.37	70.49	30.29	30.50	70.55	70.69

mance indicates reduced dependence on obfuscated gradients and better security under incomplete information. This evaluation is thus essential for assessing deployable robustness, transfer resistance, and the reliability of adversarial training in real-world threat models and systems. We test the robustness performance under the transfer-based black-box attacks.

We first evaluate a naturally trained PreActResNet-18 [24] under adversarial attacks. Its robust accuracies under PGD-100 (ℓ_∞), CW-100 (ℓ_∞), PGD-100 (ℓ_2), and CW-100 (ℓ_2) are 2.34%, 2.85%, 16.73%, and 16.22%, respectively. Then, we transfer the adversarial examples to WRN-34-10 [51]. Table 14 illustrates the robustness evaluation results that the performance of the models trained by Muon is considerable.

Similar settings are implemented on WRN-34-20 [51]. Table 15 reports black-box transfer robustness on WRN-34-20 (PreActResNet-18 as the source model). Muon consistently outperforms SGD and AdamW in nearly all settings, with especially large margins under ℓ_1 and ℓ_2 training. Notably, Muon maintains strong last-checkpoint robustness, achieving 85.10/84.96 under ℓ_∞ transfer attacks for ℓ_∞ training and 90.35/90.32 under ℓ_2 transfer attacks for ℓ_2 training. These results indicate that Muon’s gains are not limited to white-box optimization paths, but generalize to transferred adversarial examples, suggesting stronger cross-model robustness and better resistance to real black-box threat models.

Table 14: The black-box transfer attack results on WRN-34-10 [51].

Norm	Opt.	Best				Last			
		PGD (ℓ_∞)	C&W (ℓ_∞)	PGD (ℓ_2)	C&W (ℓ_2)	PGD (ℓ_∞)	C&W (ℓ_∞)	PGD (ℓ_2)	C&W (ℓ_2)
$\ell_\infty + \ell_1$	SGD	74.56	74.32	77.06	76.97	77.97	78.08	80.20	80.19
	AdamW	71.76	71.58	74.17	74.05	74.39	74.34	77.35	77.30
	Muon	68.68	68.45	71.80	71.72	82.06	81.96	84.14	84.03
ℓ_∞	SGD	76.38	76.27	78.52	78.43	79.48	79.32	81.23	81.29
	AdamW	66.64	66.58	68.37	68.40	68.44	68.63	70.66	70.78
	Muon	79.83	79.66	81.72	81.65	83.40	83.44	84.96	85.06
ℓ_1	SGD	41.90	41.69	45.52	45.57	79.50	79.22	82.61	82.46
	AdamW	59.98	59.85	63.61	63.66	68.60	68.50	73.46	73.60
	Muon	72.50	71.71	76.91	76.90	83.30	82.90	86.66	86.60
ℓ_2	SGD	70.98	70.94	74.47	74.29	83.82	83.93	86.29	86.21
	AdamW	66.00	65.94	70.75	70.88	81.81	81.66	84.65	84.61
	Muon	86.86	86.74	89.07	88.98	86.86	86.71	89.19	89.10

Table 15: The black-box transfer attack results on WRN-34-20 [51].

Norm	Opt.	Best				Last			
		PGD (ℓ_∞)	C&W (ℓ_∞)	PGD (ℓ_2)	C&W (ℓ_2)	PGD (ℓ_∞)	C&W (ℓ_∞)	PGD (ℓ_2)	C&W (ℓ_2)
$\ell_\infty + \ell_1$	SGD	70.67	70.51	73.52	73.61	79.19	78.90	81.37	81.38
	AdamW	68.34	68.23	70.95	70.98	68.34	68.23	70.95	70.97
	Muon	72.05	71.79	75.00	74.98	84.35	84.13	85.73	85.54
ℓ_∞	SGD	72.19	71.94	74.39	74.30	80.72	80.61	82.30	82.38
	AdamW	69.47	69.45	71.50	71.47	71.23	71.31	73.35	73.39
	Muon	78.82	78.48	80.66	80.56	85.10	84.96	86.48	86.42
ℓ_1	SGD	49.58	49.40	54.09	54.06	80.49	80.19	83.99	83.96
	AdamW	62.73	62.49	66.79	66.85	76.56	76.20	80.46	80.38
	Muon	84.49	84.15	87.64	87.64	84.15	83.76	87.49	87.52
ℓ_2	SGD	84.78	84.56	87.20	87.03	85.13	84.70	87.29	87.36
	AdamW	81.56	81.56	84.02	83.92	81.11	81.03	83.82	83.67
	Muon	88.19	88.11	90.26	90.21	88.30	88.15	90.35	90.32